Journal of Biomedical Optics

BiomedicalOptics.SPIEDigitalLibrary.org

Microvascular quantification based on contour-scanning photoacoustic microscopy

Chenghung Yeh
Brian Soetikno
Song Hu
Konstantin I. Maslov
Lihong V. Wang

SPIE.

Microvascular quantification based on contour-scanning photoacoustic microscopy

Chenghung Yeh,[a] Brian Soetikno,[a] Song Hu,[a,b] Konstantin I. Maslov,[a] and Lihong V. Wang[a,*]
[a]Washington University in St. Louis, Department of Biomedical Engineering, Optical Imaging Laboratory, One Brookings Drive, St. Louis, Missouri 63130, United States
[b]University of Virginia, Department of Biomedical Engineering, PO Box 800759, Charlottesville, Virginia 22908, United States

Abstract. Accurate quantification of microvasculature remains of interest in fundamental pathophysiological studies and clinical trials. Current photoacoustic microscopy can noninvasively quantify properties of the microvasculature, including vessel density and diameter, with a high spatial resolution. However, the depth range of focus (i.e., focal zone) of optical-resolution photoacoustic microscopy (OR-PAM) is often insufficient to encompass the depth variations of features of interest—such as blood vessels—due to uneven tissue surfaces. Thus, time-consuming image acquisitions at multiple different focal planes are required to maintain the region of interest in the focal zone. We have developed continuous three-dimensional motorized contour-scanning OR-PAM, which enables real-time adjustment of the focal plane to track the vessels' profile. We have experimentally demonstrated that contour scanning improves the signal-to-noise ratio of conventional OR-PAM by as much as 41% and shortens the image acquisition time by 3.2 times. Moreover, contour-scanning OR-PAM more accurately quantifies vessel density and diameter, and has been applied to studying tumors with uneven surfaces. [DOI: 10.1117/1.JBO.19.9.096011]

Keywords: optical-resolution photoacoustic microscopy; contour scanning; raster scanning; tumors; melanoma; brain; segmentation; *z*-stack; diameter; signal-to-noise ratio.

Paper 140366R received Jun. 9, 2014; revised manuscript received Aug. 21, 2014; accepted for publication Aug. 27, 2014; published online Sep. 15, 2014.

The microcirculation of the cardiovascular system consists of capillary vessels where oxygen, glucose, amino acids, other nutrients, and waste are exchanged.[1] Angiogenesis is the process whereby new blood vessels are formed from pre-existing vessels to supply tissue with oxygen and nutrition.[2] Both microcirculation and angiogenesis play crucial roles in pathologic processes, including tumor growth, metastasis, and ischemia.[3,4] Thus, *in vivo* characterization of angiogenesis and microcirculation are of particular significance. Many clinical trials have used anti-angiogenic therapies to delay the progression of certain cancers, and microvessel density is one of the most useful prognostic indicators of angiogenic activity.[5] Over the last century, intravital microscopy (IVM) has been the gold standard in quantitative measurements of tumor angiogenesis.[6–8] However, IVM requires surgical preparation and lacks depth information about the microvascular structure. Two-photon microscopy (TPM) and optical microangiography (OMAG) eliminate the need for invasive preparation and enable functional microvasculature imaging.[9,10] However, TPM imaging relies on exogenous fluorescent agents for contrast. Although OMAG enables intrinsic imaging on the microvascular level, it encounters challenges in imaging functional information, such as the oxygen saturation of hemoglobin, and its sensitivity is not yet sufficient to image single blood cells.

In contrast, optical-resolution photoacoustic microscopy (OR-PAM) is capable of high-resolution, noninvasive, label-free, and functional imaging of the microvasculature *in vivo*.[11–14] Capitalizing on hemoglobin as an endogenous contrast, OR-PAM has enabled multiparametric quantification of the microvasculature, including vessel diameter, the concentration and oxygenation of hemoglobin, blood flow, the metabolic rate of oxygen, and the pulse wave velocity of blood.[15,16] However, the depth range of focus (i.e., focal zone) of conventional OR-PAM is often insufficient to encompass the depth variations of features of interest, particularly the vasculature in the brain and bumpy tumors. As a result, the image quality of out-of-focus blood vessels is compromised due to poor spatial resolution and a low signal-to-noise ratio (SNR).

Conventional OR-PAM relies upon two-dimensional (2-D) raster scanning, whereby the optical and acoustic objectives are mechanically scanned in a horizontal (i.e., $x-y$) plane. Raster scanning serially at different focus depths, termed z-stack scanning, extends the focal zone, similar to 2-D optical sections in z-stack confocal and two-photon microscopy.[17,18] The collection of images is combined to form a single three-dimensional (3-D), high-quality, in-focus image over an extended depth range. However, the image acquisition time of z-stack scanning increases proportionally with the depth of the region of interest, which could lead to undesirably slow imaging for *in vivo* studies. To overcome this limitation, Zhang et al. proposed and developed raster scanning with axial adjustment for acoustic resolution PAM.[19] However, instead of simultaneously adjusting the axial and $x-y$ positions of the objective, the ultrasonic transducer was moved from one measurement point to another, with pauses to adjust the axial position. This procedure was repeated for each $x-y$ position, resulting in an irregular scanning speed depending on the amount of axial adjustment. Correspondingly, for a 10×8.2 mm^2 image area with a motor

*Address all correspondence to: Lihong V. Wang, E-mail: lhwang@wustl.edu

0091-3286/2014/$25.00

step size of 50 μm, scanning took up to 130 min, too long to capture rapid physiological changes.

In this letter, we report the development and application of continuous 3-D motorized contour-scanning OR-PAM for *in vivo* imaging through uneven tissue surfaces. We experimentally evaluate the improvements in spatial resolution, SNR, and acquisition time over conventional raster scanning and z-stack scanning. With these advances, we greatly improve the accuracy of vessel density and diameter quantification.

In our conventional OR-PAM system [Fig. 1(a)],[20] the laser beam from a solid-state laser (SPOT, Elforlight; 532 nm wavelength, Northants, United Kingdom) is reshaped by an iris (ID25SS, Thorlabs; 2-mm aperture size, New Jersey), spatially filtered through a 50-μm-diameter pinhole (P50C, Thorlabs), and focused by a condenser lens (LA1131, Thorlabs) into a single-mode fiber (LMA-10, NKT Photonics, New Jersey). A tunable neutral density filter (NDC-50C-2M, Thorlabs) regulates the intensity of the laser beam incident on the fiber tip. The fiber output is collimated by a microscope objective (RMS4X, Thorlabs), reflected by a mirror, and focused by another identical objective. An acoustic-optical beam combiner with two prisms and an intervening layer of silicone oil concentrically aligns the optical and ultrasonic foci. The generated photoacoustic wave is detected by an ultrasonic transducer (V214-BB-RM, Olympus-NDT, Massachusetts) through an acoustic lens engraved in the bottom surface of the beam combiner. The detected photoacoustic wave is amplified by two cascaded electrical amplifiers with a combined gain of 48 dB (ZFL 500LN, Mini-Circuits, New York) and digitized by a high-speed digitizer (ATS9350, Alazar Tech Inc., Pointe-Claire, Canada). The scanning head is translated in the $x-y$ plane by two motorized linear stages (PLS-85, PI miCos, Eschbach, Germany) and in the z-direction by a third linear stage (VT-21 S, PI miCos).

Contour scanning requires real-time vertical adjustment of the optical-acoustic dual foci at each $x-y$ position. We used a three-step method to approximate the 2-D surface function for the scanning stage to follow. As shown in Fig. 1(b), our method begins by rapidly assessing the height variations of the tissue surface by raster scanning the region of interest with a large y-step size of 50 μm. A fine x-step size of 2.5 μm was chosen to precisely delineate the depth variation along each cross-sectional scan (i.e., B-scan), where the maximum-amplitude position along each A-line is identified and then fitted with a b-spline function in MATLAB® (R2012b, MathWorks, Massachusetts) [Fig. 1(c)]. These fitting curves are then linearly interpolated along the y-direction to reduce their spacing to 5 μm [Fig. 1(d)]. Collectively, the resulting curves approximate a 2-D surface function, which simultaneously guides the positioning of the three motorized scanning stages through LabView (Version 11, National Instruments, Austin).

Contour-scanning OR-PAM was quantitatively compared with both conventional raster-scanning and z-stack scanning OR-PAM (120 μm section thickness) in terms of lateral resolution and SNR. The full width at half maximum lateral resolution of our OR-PAM system was experimentally measured using an Air Force resolution test target (04TRN003, CVI MellesGriot). Since the light intensity distribution is approximately Gaussian, the degradation of lateral resolution along the z-direction is expected to follow the increase of the Gaussian beam width, $w(z) = w_0\sqrt{1+(z/z_R)^2}$. As shown in Fig. 2(a), the illumination has a focal diameter of 2.22 μm, which approximately corresponds to the theoretical diffraction-limited optical focal diameter of 2.04 μm. For z-stack scanning, the lateral resolution curve repeats that of conventional raster scanning every 120 μm. In contrast, contour scanning enables real-time z-adjustment of the imaging head to follow the tissue surface. Thus, the lateral

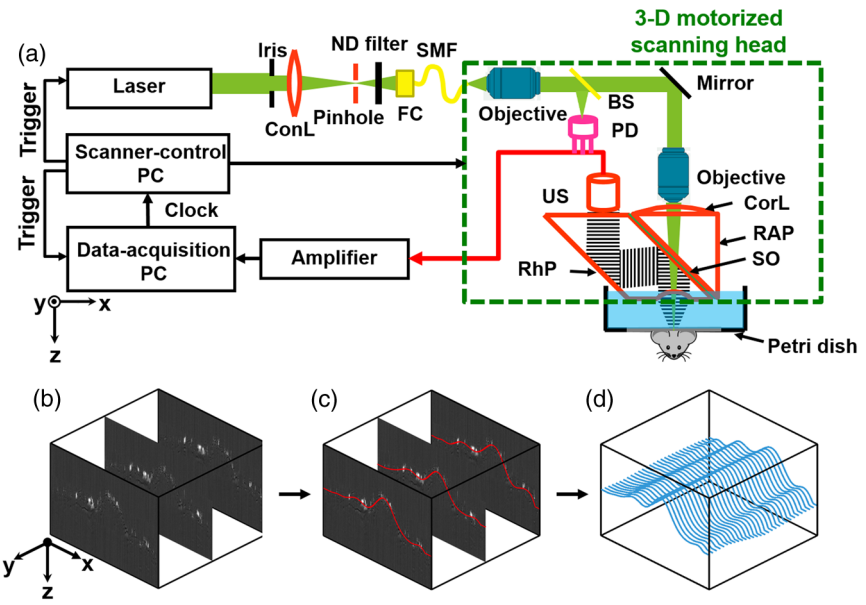

Fig. 1 Contour scanning photoacoustic microscopy. (a) Schematic diagram of continuous three-dimensional (3-D) motorized contour-scanning optical-resolution photoacoustic microscopy (OR-PAM). ConL, condenser lens; ND, neutral density; FC, fiber collimator; SMF, single-mode fiber; BS, beam splitter; PD, photodiode; CorL, correction lens; RAP, right-angle prism; SO, silicone oil; RhP, rhomboid prism; US, ultrasonic transducer. The three-step contour scanning method is illustrated as follows. (b) Quick B-scans every 50 μm. (c) Polynomial fit (red) of the maximum amplitude positions along each A-line in each B-scan. (d) Refinement of the curves (blue) with linear interpolation of (c) along the y-direction to approximate a two-dimensional (2-D) surface.

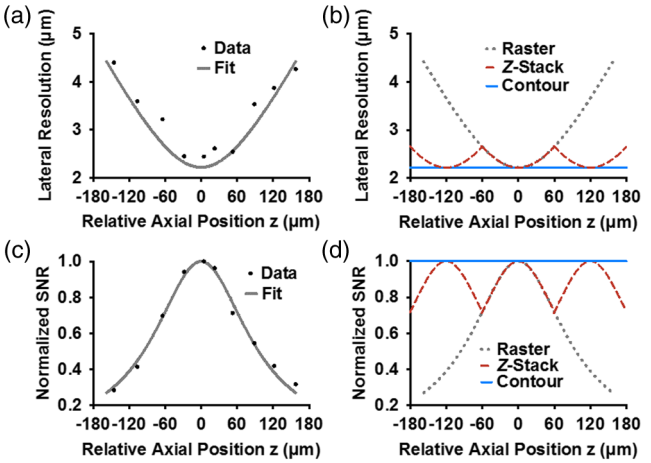

Fig. 2 Resolution and signal-to-noise ratio (SNR) comparison. (a) Lateral resolution versus axial position. Solid curve: fitting by Gaussian beam formula. (b) Expected lateral resolution versus axial position of contour (blue dashed line), *z*-stack (red dashed line), and raster scan (gray dotted line) based on the fitted data in (a). (c) Acoustic-amplitude SNR versus axial position for raster scan. (d) Expected acoustic-amplitude SNR versus axial position of contour, *z*-stack, and raster scans based on the fitted data in (c).

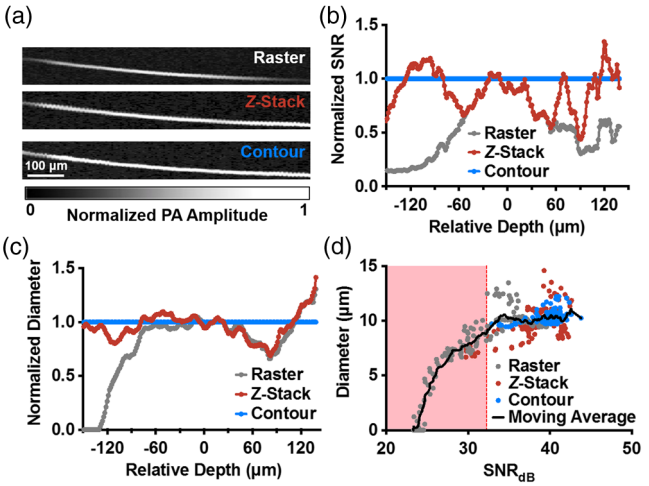

Fig. 3 Resolution and acoustic-amplitude SNR comparison by imaging a carbon fiber. (a) Top-view maximum amplitude projection (MAP) images of the carbon fiber. (b) Acoustic-amplitude SNR and imaged fiber diameter as a function of fiber depth. (c) Imaged fiber diameter as a function of depth. (d) Diameter as a function of SNR in units of decibels.

resolution of contour-scanning OR-PAM remains optimal across the entire depth range [Fig. 2(b)]. Based on our computation, the arithmetic average lateral resolution of contour-scanning OR-PAM is 24% finer than raster-scanning OR-PAM and 7% finer than *z*-stack scanning OR-PAM over the depth range from -120 to $+120$ μm. Similarly, we compared the SNRs obtained by the three implementations [Figs. 2(c) and 2(d)]. Over the depth range from -120 to $+120$ μm, the average SNR of contour-scanning OR-PAM is 41% higher than that of raster-scanning OR-PAM and 12% higher than that of *z*-stack scanning OR-PAM.

To experimentally compare the three scanning methods, we imaged an obliquely oriented carbon fiber in water [Fig. 3(a)]. The SNR normalized by the measurements from contour scanning is plotted as a function of the depth of the fiber [Fig. 3(b)]. Similarly, we also plotted the normalized imaged fiber diameter as a function of depth [Fig. 3(c)]. Diameter was measured by the following procedure. First, a regional thresholding algorithm was applied to the photoacoustic image of the fiber to convert it to a binary mask.[21] Second, a Euclidean distance transform was applied to the binary mask to form a map, where each pixel value represents the Euclidean distance to the closest zero pixel. Finally, the numerical value at the centerline of map was recorded and multiplied by 2 to obtain the diameter for each cross-section of the fiber. With contour scanning, the SNR and the imaged diameter of the carbon fiber were preserved across the entire depth range. *Z*-stack scanning showed a periodic change in both SNR and diameter approximately every 120 μm, reflecting our predetermined section thickness. Over the depths from -120 to $+120$ μm, the average amplitude acquired by contour scanning was 15 and 69% higher than that obtained by *z*-stack scanning and raster scanning, respectively. Over the same depth range, the average diameter acquired by *z*-stack OR-PAM was 8% greater than that obtained by raster scanning, but 6% less than that obtained by contour scanning.

Interestingly, we observed that, besides the loss of resolution, the measured fiber diameter was also affected by the degradation in SNR. While lower resolution increases the measured diameter, a lower SNR decreases the measured diameter by making signals indistinguishable from the background. To quantitatively investigate the impact of SNR on diameter measurement, we plotted the measured fiber diameter versus the SNR in the unit of decibels [Fig. 3(d)]. The mean, μ, of measured diameters for contour scanning was 10.34 μm, and the standard deviation, σ, was 0.47 μm. Here, we defined a cutoff value as $\mu - 3\sigma$, equating to 8.93 μm and corresponding to an SNR of 32 dB. When the SNR fell below this cutoff point due to the out-of-focus effect, the regional-thresholding algorithm became incapable of correctly distinguishing the background from the fiber, and there was a corresponding decrease in the measured diameter, resulting in a measurement error.[22] These results suggest that the contour scanning–induced improvement in the SNR is particularly important in the quantitative study of vascular anatomy.

For *in vivo* exploration of SNR and vessel diameter, a 12×12 mm^2 region in a living mouse ear was consecutively imaged by *z*-stack and contour-scanning OR-PAM. For *z*-stack scanning, four raster scans were conducted with a 120 μm sectioning interval to cover the entire thickness of the ear [Fig. 4(a)]. The four sections were combined and converted into a single maximum amplitude projection (MAP) image [Fig. 4(b)]. A single contour scan was performed, resulting in an MAP image of the same region [Fig. 4(c)]. For each of the images, the vessel diameter (D) at each pixel position was quantified and classified into three categories: $D > 35$ μm (blue), 35 μm $> D > 10$ μm (red), and $D < 10$ μm (green) [Fig. 4(d)]. The pixel count is normalized by the highest pixel count obtained by the *z*-stack scanning. Due to its superior SNR, contour scanning scores most pixels among all scanning mechanisms.

We also performed an *in vivo* SNR comparison of the images shown in Fig. 4 based on vessel segmentation.[23] The major arterial and vein trees were identified, segmented, labeled, and divided into subtrees [Fig. 5(a)]. To obtain the SNR, the average photoacoustic amplitude within each subtree was quantified and divided by the noise level, which was estimated using

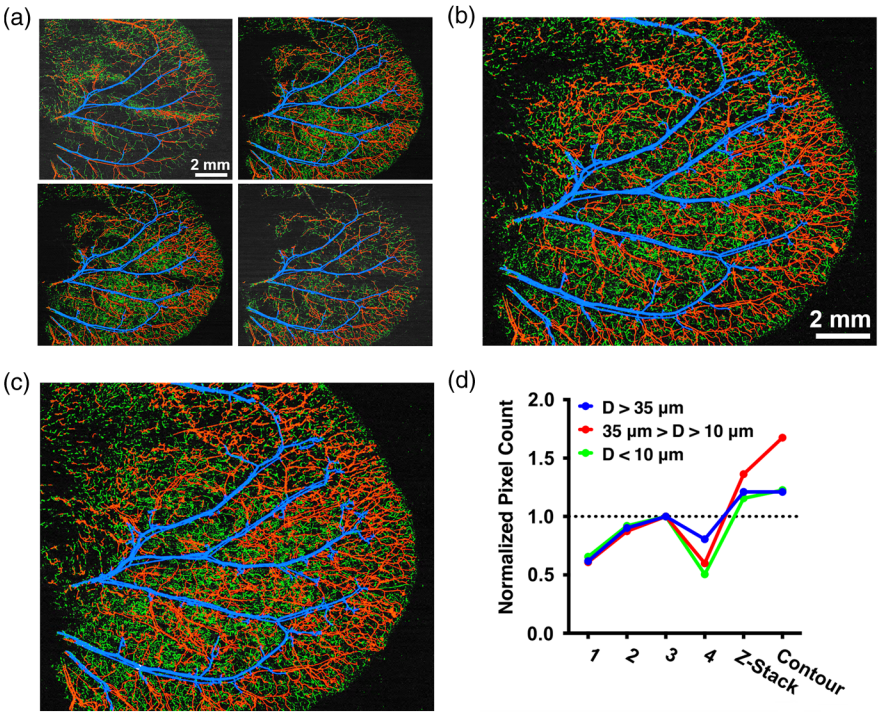

Fig. 4 Comparison of *in vivo* raster, *z*-stack, and contour-scanning OR-PAM. (a) *Z*-stack consisting of four 2-D raster scans of a mouse ear at 120 μm intervals. Labeled by color based on diameter: $D > 35$ μm (blue), 35 μm $> D >$ 10 μm (red), and $D < 10$ μm (green). (b) MAP of the entire *z*-stack. (c) MAP of the 3-D contour image. (d) Normalized pixel counts for each vessel-size category obtained by each of the four raster scans, the *z*-stack scan, and the contour scan.

the standard deviation of the background photoacoustic amplitude. The SNR of each subtree was plotted versus the scanning mode and normalized by the highest SNR obtained by the *z*-stack scanning [Fig. 5(b)]. In all cases, the contour scan had subtree SNRs that were greater than or approximately equal to the highest SNR from the *z*-stack. The average SNR improvements for the contour scan and *z*-stack scan over the best single raster scan were $13.5\% \pm 7.9\%$ and $6.2\% \pm 5.8\%$, respectively [Fig. 5(c)]. On average, the SNR of the contour scan was 6.9% higher than that of the *z*-stack.

The difference in SNR between *z*-stack and contour scanning addressed the discrepancy in the measurements of vessel diameter using the two methods [Fig. 4(d)]. For large vessels ($D > 35$ μm), no difference was observed between *z*-stack and contour scanning, since these vessels had high volumes of hemoglobin and, thus, high SNRs. For medium-sized vessels (35 μm $> D >$ 10 μm), we observed a reduced number of pixels counted from *z*-stack scanning compared to contour scanning. Interestingly, for small-sized vessels ($D < 10$ μm), where *z*-stack scanning was expected to have considerably fewer pixels than contour scanning, the pixel counts were similar. We attributed this observation to measurement error due to loss of SNR. As shown previously, *z*-stack scanning did not have as high SNR improvements as contour scanning; therefore, some medium-sized vessels fell below the SNR threshold, were measured as having a smaller diameter than the true value, and were, therefore, miscounted into the small-sized vessel category. In all size categories, *z*-stack and contour scanning had more total pixels than raster scanning did, with contour scanning having the highest overall. Here, our analysis has demonstrated that contour scanning has advantages in SNR and in accurate quantification of vessel diameter and vessel density, which has been important for *in vivo* studies involving angiogenesis and neovascularization.[4,5]

To demonstrate the advantage of contour-scanning OR-PAM in acquisition time, we imaged a mouse ear with an early-stage renal tumor (786-O cell line) with a maximum thickness of ~560 μm. Stacking the four sectional scans [Fig. 6(a)] led to a clear MAP image of the whole ear [Fig. 6(b)], which took ~80 min. In comparison, a 3-D contour scan obtained a high-resolution tumor-bearing ear image of the same quality, if not better, within only ~25 min [Fig. 6(c)]. Therefore, the acquisition time of the contour scan was 3.2 times faster than the *z*-stack scan. Notably, the benefit in image acquisition time becomes even more significant when imaging a well-developed tumor (typical thickness: >2 mm). In such a situation, the image acquisition time can be reduced 20-fold. To cover the depth of significantly large tumors, the focus of contour-scanning OR-PAM can be offset and multiple contour scans can be performed, constituting a *z*-stack of contour scans. In such situations, *z*-stack contour-scanning OR-PAM still acquires images faster than *z*-stack scanning, as long as the tumor thickness is larger than the depth range of focus of our PAM system.

In conclusion, we have developed continuous 3-D motorized contour-scanning OR-PAM to address the out-of-focus issue arising from uneven tissue surfaces. The advantages of contour-scanning OR-PAM in spatial resolution, SNR, and imaging speed were experimentally demonstrated. In addition to maintaining optimal lateral resolution and SNR within extended depth ranges, contour scanning ensures accurate measurements of vessel density and diameter. Measurements of parameters

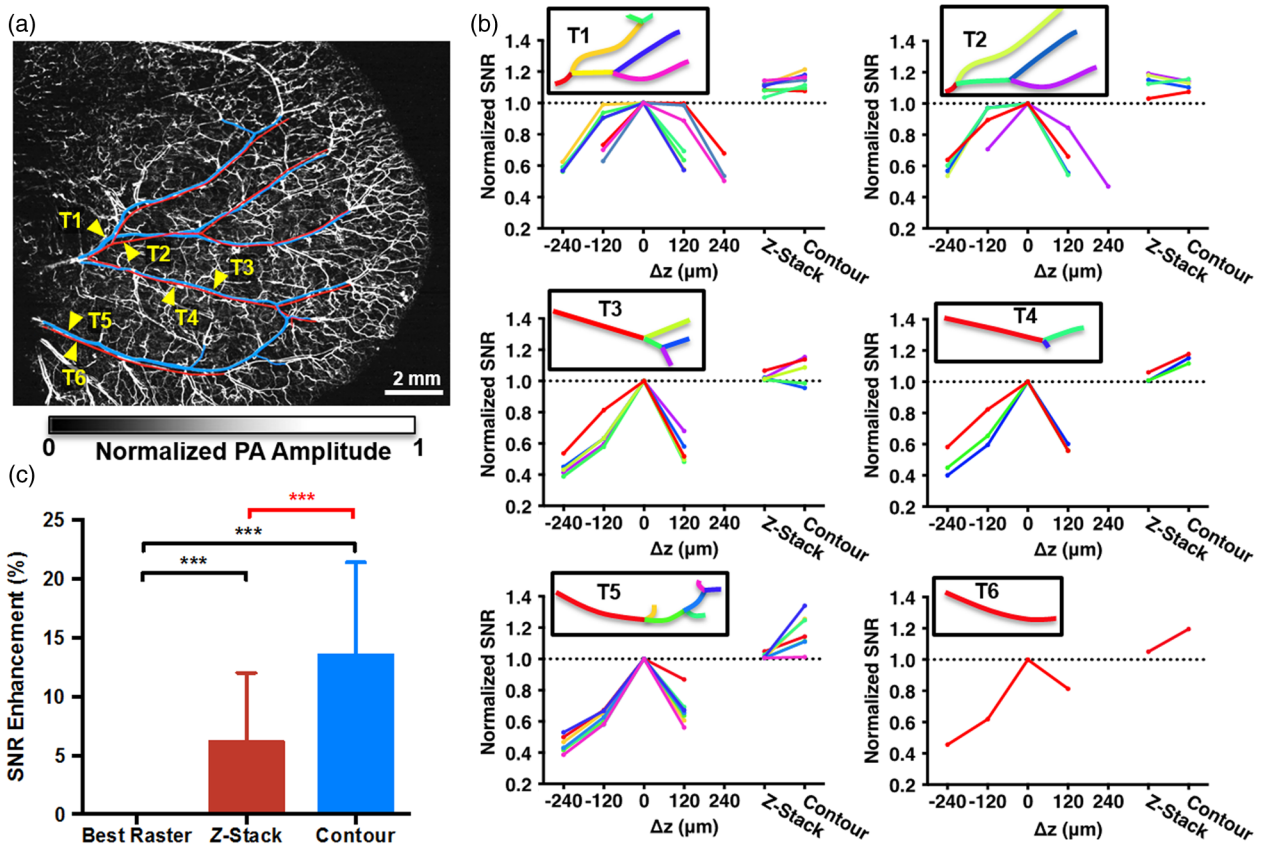

Fig. 5 SNR comparison between scans shown in Fig. 4. (a) Vessel segmentation of major artery (red) and vein (blue) trees. Six identified trees (T1 to T6) indicated by yellow arrows. (b) Averaged SNR from subtrees of T1 to T6 normalized by the maximum SNR from the *z*-stack. Black box: trees vectorized and subtrees color-coded to match corresponding plotted lines. Each different color represents a segment. (c) Comparison of the SNR enhancement between the three scans. Statistics: one sample *t* test (black), paired student's *t* test (red), ***p value <0.001, $n = 28$ branches. Data are presented as mean ± standard deviation.

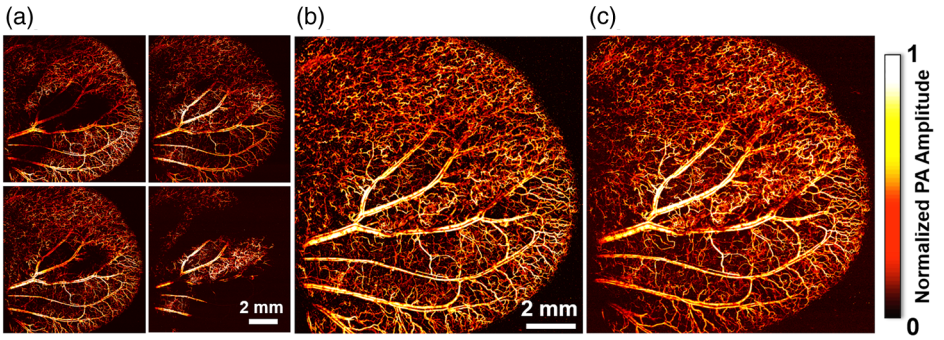

Fig. 6 Melanoma tumor in a mouse ear imaged with raster scanning and contour scanning. (a) *Z*-stack consisting of four MAPs of raster scans spaced 120 μm apart in the *z*-direction. (b) $X - Y$ MAP of the entire *z*-stack. (c) $X - Y$ MAP of the contour scan image.

such as flow speed, the metabolic rate of oxygen, and pulse wave velocity, which all depend on vessel diameter, are also expected to improve with contour scanning. Achieving high-resolution imaging of uneven surfaces without time-consuming *z*-stack scans makes contour-scanning OR-PAM a promising tool for tumor and brain research. This implementation is expected to have a particular impact on subwavelength OR-PAM,[24] whose relatively small depth of focus (~1 μm) would require a correspondingly greater number of scans.

Acknowledgments

The authors appreciate the close reading of the manuscript by Professor James Ballard. We also thank Wenxin Xing, Jinyang Liang, Yong Zhou, and Lidai Wang for helpful discussions. This work was sponsored by National Institutes of Health Grants DP1 EB016986 (NIH Director's Pioneer Award), R01 CA159959, R01 CA186567 (NIH Director's Transformative Research Award), and R01 EB016963. L.V.W. has financial

interests in Microphotoacoustics Inc. and Endra Inc., neither of which supported this work. K.I.M. has a financial interest in Microphotoacoustics Inc.

References

1. R. E. Klabunde, *Cardiovascular Physiology Concepts*, Lippincott Williams & Wilkins, New York (2005).
2. A. Birbrair et al., "Type-2 pericytes participate in normal and tumoral angiogenesis," *Am. J. Physiol.: Cell Physiol.* **307**, C25–C38 (2014).
3. P. Vajkoczy, A. Ullrich, and M. D. Menger, "Intravital fluorescence videomicroscopy to study tumor angiogenesis and microcirculation," *Neoplasia* **2**(1–2), 53–61 (2000).
4. S. S. Oladipupo et al., "Conditional HIF-1 induction produces multistage neovascularization with stage-specific sensitivity to VEGFR inhibitors and myeloid cell independence," *Blood* **117**(15), 4142–4153 (2011).
5. L. Hlatky, P. Hahnfeldt, and J. Folkman, "Clinical application of antiangiogenic therapy: microvessel density, what it does and doesn't tell us," *J. Natl. Cancer Inst.* **94**(12), 883–893 (2002).
6. S. Brem, R. Cotran, and J. Folkman, "Tumor angiogenesis: a quantitative method for histologic grading," *J. Natl. Cancer Inst.* **48**(2), 347–356 (1972).
7. M. D. Menger and H.-A. Lehr, "Scope and perspectives of intravital microscopy-bridge over from in vitro to in vivo," *Immunol. Today* **14**(11), 519–522 (1993).
8. H.-A. Lehr et al., "Dorsal skinfold chamber technique for intravital microscopy in nude mice," *Am. J. Pathol.* **143**(4), 1055–1062 (1993).
9. L. An, J. Qin, and R. K. Wang, "Ultrahigh sensitive optical microangiography for in vivo imaging of microcirculations within human skin tissue beds," *Opt. Express* **18**(8), 8220–8228 (2010).
10. A. Y. Shih et al., "Two-photon microscopy as a tool to study blood flow and neurovascular coupling in the rodent brain," *J. Cereb. Blood Flow Metab.* **32**(7), 1277–1309 (2012).
11. Z. Xie et al., "Laser-scanning optical-resolution photoacoustic microscopy," *Opt. Lett.* **34**(12), 1771–1773 (2009).
12. Y. Su et al., "A photoacoustic tomography system for imaging of biological tissues," *J. Phys. D: Appl. Phys.* **38**(15), 2640 (2005).
13. L. V. Wang and S. Hu, "Photoacoustic tomography: in vivo imaging from organelles to organs," *Science* **335**(6075), 1458–1462 (2012).
14. S.-L. Chen et al., "In vivo flow speed measurement of capillaries by photoacoustic correlation spectroscopy," *Opt. Lett.* **36**(20), 4017–4019 (2011).
15. J. Yao et al., "Label-free oxygen-metabolic photoacoustic microscopy in vivo," *J. Biomed. Opt.* **16**(7), 076003 (2011).
16. C. Yeh et al., "Photoacoustic microscopy of blood pulse wave," *J. Biomed. Opt.* **17**(7), 0705041 (2012).
17. M. J. Miller et al., "Autonomous T cell trafficking examined in vivo with intravital two-photon microscopy," *Proc. Natl. Acad. Sci.* **100**(5), 2604–2609 (2003).
18. A. Richter-Dahlfors, A. M. Buchan, and B. B. Finlay, "Murine salmonellosis studied by confocal microscopy: Salmonella typhimurium resides intracellularly inside macrophages and exerts a cytotoxic effect on phagocytes in vivo," *J. Exp. Med.* **186**(4), 569–580 (1997).
19. H. F. Zhang et al., "In vivo volumetric imaging of subcutaneous microvasculature by photoacoustic microscopy," *Opt. Express* **14**(20), 9317–9323 (2006).
20. S. Hu, K. Maslov, and L. V. Wang, "Second-generation optical-resolution photoacoustic microscopy with improved sensitivity and speed," *Opt. Lett.* **36**(7), 1134–1136 (2011).
21. P. S. Tsai et al., "Correlations of neuronal and microvascular densities in murine cortex revealed by direct counting and colocalization of nuclei and vessels," *J. Neurosci.* **29**(46), 14553–14570 (2009).
22. H. Bouma et al., "Unbiased vessel-diameter quantification based on the FWHM criterion," *Proc. SPIE* **6512**, 65122N (2007).
23. B. Soetikno et al., "Vessel segmentation analysis of ischemic stroke images acquired with photoacoustic microscopy," *Proc. SPIE* **8223**, 822345 (2012).
24. C. Zhang et al., "Reflection-mode submicron-resolution in vivo photoacoustic microscopy," *J. Biomed. Opt.* **17**(2), 020501 (2012).

Chenghung Yeh received his BS in physics from National Taiwan University, Taiwan. He is currently a PhD student at Washington University in St. Louis, Missouri, USA. His research interests focus on the application of photoacoustic microscopy in biological and medical study.

Brian Soetikno received his BS in biomedical engineering from Washington University in St. Louis, and is currently a second-year MD/PhD student at Northwestern University, Chicago, USA. His research interests focus on investigating and diagnosing diseases using functional optical imaging.

Song Hu received his BS and MS degrees in electronic engineering at Tsinghua University in 2002 and 2005, respectively. After receiving his PhD in biomedical engineering at Washington University in St. Louis in 2010, he continued postdoctoral research with Dr. Lihong Wang, extending his doctoral work to multicontrast photoacoustic microscopy of vascular and metabolic biology. He joined the Department of Biomedical Engineering at the University of Virginia as an assistant professor in May of 2013.

Konstantin I. Maslov graduated from Moscow Institute of Physics and Technology, Moscow, Russia, and received a PhD in physical acoustics from Moscow State University, Russia, in 1993. Currently he is a research associate professor in the Biomedical Engineering Department at Washington University in St. Louis, Missouri. His area of interest includes optical, photoacoustic and acoustic imaging, and optical and photoacoustic spectroscopy.

Lihong V. Wang earned his PhD degree at Rice University, Houston, Texas, and currently holds the Gene K. Beare Distinguished Professorship of Biomedical Engineering at Washington University in St. Louis. His laboratory invented or discovered functional photoacoustic tomography, dark-field confocal photoacoustic microscopy (PAM), optical-resolution PAM, photoacoustic Doppler effect, photoacoustic reporter gene imaging, focused scanning microwave-induced thermoacoustic tomography, the universal photoacoustic or thermoacoustic reconstruction algorithm.